J. Plasma Physics (2006), *vol.* 72, *part* 4, *pp.* 525–546. © 2006 Cambridge University Press
doi:10.1017/S0022377805004162 First published online 11 January 2006 Printed in the United Kingdom

Influence of the Ramsauer–Townsend minimum on the electron energy distribution function and electron transport in xenon

VIDA ŽIGMAN

Nova Gorica Polytechnic, Nova Gorica, PO Box 301, Slovenia
(vida.zigman@p.ng-si)

(Received 17 February 2005 and accepted 4 May 2005)

Abstract. The electron distribution function in xenon in the low-energy region comprising the Ramsauer–Townsend minimum was obtained by solving the Boltzmann equation in the hydrodynamic approximation, for electric field to gas density ratios E/N in the range (0.01, 3) Td. The distortion of the electron distribution function due to the minimum is analysed and correlated to the behaviour of the electron transport coefficients: the drift velocity W_d and the ratio of the transverse and longitudinal diffusion coefficient to mobility, D_T/μ and D_L/μ. The results are discussed in view of the different theoretical and experimental cross-section data used.

1. Introduction

This paper reports a detailed examination of the electron distribution function (edf) and related electron transport parameters, i.e. the mean energy, the drift velocity, the transverse and longitudinal diffusion coefficient to mobility ratio D_T/μ and D_L/μ in a xenon low-temperature weakly ionized plasma in a dc electric field over the range of the Ramsauer–Townsend minimum (RTM) in elastic electron scattering.

Electron kinetics is known to play a central role in weakly ionized low-temperature plasmas. Due to the low degree of ionization the plasma electrons usually exhibit a pronounced non-equilibrium energy distribution, its determination being one of the main concerns in the kinetic modelling of gas discharges [1–5].

In the field of low-energy electron–atom collisions, theory and swarm experiments are in a competitive effort to improve the reliability and consistency of cross-section data. The electron swarm procedure for unfolding electron–neutral (e–n) cross-sections from measured transport coefficients relies on the connection between the electron properties on the microscopic and macroscopic scales, provided by the edf. It is the edf that relates two completely different approaches to the same objective – the description of the e–n interaction: the theoretical one, searching for the rigorous quantum mechanical explanation of the electron–atom scattering process, and the experimental one, measuring electron transport parameters through a variety of sophisticated techniques in order to evolve the collision cross-sections. The edf is necessary to the first approach to reproduce the transport parameters

https://doi.org/10.1017/S0022377805004162 Published online by Cambridge University Press

from calculated cross-sections [6], as it is indispensable to the second, to reconstruct from measured quantities the set of optimal collision data [7–10].

Since the early works of Frost and Phelps [11], Skullerud [12] and Parker and Lowke [13, 14] which traced the theoretical bases of investigation into the overlapping regions of plasma kinetic theory and electron swarms, the behaviour of electrons in xenon has attracted continuous attention [15]. Methods for solving the Boltzmann equation, using both the traditional two-term and the subsequent multiterm expansion of the velocity distribution function in spherical harmonics (e.g. [16]), as well as the alternative Monte Carlo (MC) simulations [17, 18] have extensively included swarms and plasmas in inert gases, xenon in particular, e.g. [7, 10, 19–21].

In technological plasmas xenon is one of the favorite filling gases, unavoidable in light sources, excimer lasers, gas proportional scintillation counters and plasma displays. However, investigations of gas discharges which operate on xenon as an efficient ultraviolet emitter [20–22] generally focus on the energy region where excitation and Penning ionization (xenon in mixture with other inert gases) play a dominant role, undermining to some extent the low-energy region, through which the primary energy input is achieved.

As a high-Z target with closed-shell structure, xenon exhibits the RTM in elastic scattering of electrons at 0.6–0.7 eV, with the scattering cross-section varying over two orders of magnitude in the vicinity of the minimum (e.g. [23]). The pronounced energy dependence of the elastic cross-section has been a challenge to both aspects, theoretical and experimental, in determining the absolute cross-sections values. However, in understanding electron transport on the macroscopic scale, the relation between the cross-sections and the transport coefficients is generally emphasized, while much less attention has been devoted to the edf itself. This is, at least partly, due to techniques other than the multiterm solution of the Boltzmann equation, where the velocity moments of the edf rather than the edf itself are directly evaluated, as in the moment method of Lin et al. [24] or the Fourier expansion procedure of Parker and Lowke [13].

In this paper we aim to remedy this situation and also to elucidate the macroscopic low-energy transport through the detailed structure of the energy distribution of electrons, in the region of the RTM and in xenon in particular, as the representative of heavier ('Ramsauer') inert gases. To this end the Boltzmann kinetic equation for electrons is solved in the hydrodynamic regime. The examined region of the *reduced electric field strengths* E/N (where E is the electric field strength and N is the gas number density), and the pertaining energy ranges were determined by the remarkable changes the edf goes through over the RTM with increasing E/N. On the thus specified ranges of E/N, (0.01, 3) Td (1 Td $= 10^{-21}$ V m^2), and electron energies, (0.001, 7) eV, only elastic e–Xe scattering, with rather poor energy exchange per collision, is to be taken into account. Consequently, the first two terms in the expansion of the electron distribution function in spherical harmonics in velocity space are proved to be adequate. This means that the accuracy criterion has been specified beforehand by the higher successive approximation, as recently emphasized by White et al. [25]. We, therefore, apply a well-known and extensively used method, briefly reviewed, in general, in Sec. 2, and in more detail as applied to xenon, in Sec. 3. In Sec. 4 we focus on the detailed analysis of the edf over the RTM, both as a function of electron energy and of the reduced electric field strength, and discuss the consequent behaviour of the electron transport coefficients. To

https://doi.org/10.1017/S0022377805004162 Published online by Cambridge University Press

clarify the effect of the strongly varying cross-sections with energy, in particular the impact of the position and depth of the RTM, recent evaluated and measured cross-section data have been used. The results arrived at, summarized in Sec. 5, unravel the influence of the e–Xe interaction on the edf at low energies, and correlate the characteristic features of the latter to the behaviour of the transport coefficients over the RTM.

2. Theoretical background

We outline briefly the hydrodynamic description as thoroughly formulated by Kumar and co-workers [26, 27].

The well-known Boltzmann equation for the electron velocity distribution function $g(\mathbf{v}, \mathbf{r}, t)$:

$$\frac{\partial g}{\partial t} + \mathbf{v} \cdot \nabla_r g + \frac{e\mathbf{E}}{m_\mathrm{e}} \cdot \nabla_v g = J(g) \tag{1}$$

is considered, where e and m_e denote the electron charge and mass respectively, $\mathbf{E}$ is the external electric field and J is the collision integral. At present, equation (1) has been applied to electrons in a steady-state, collision-dominated weakly ionized plasma in an external dc electric field $\mathbf{E} = -E\boldsymbol{\kappa}$ ($\boldsymbol{\kappa}$ being a unit vector along the z axis). The solution is searched by expanding the distribution in series of successive gradients in electron number density $n(\mathbf{r}, t)$ [26, 28]:

$$g(\mathbf{v}, \mathbf{r}, t) = \sum_k \mathbf{g}^k(\mathbf{v}) \cdot (\nabla_r)^k n(\mathbf{r}, t) = g^0(\mathbf{v}) n(\mathbf{r}, t) + \mathbf{g}^1(\mathbf{v}) \cdot \nabla_r n(\mathbf{r}, t) + \cdots \tag{2}$$

where the functions $\mathbf{g}^k(\mathbf{v})$ fulfil the normalization conditions

$$\int \mathbf{g}^k(\mathbf{v})\, d\mathbf{v} = \delta_{0k} \quad (k = 0, 1, 2, \dots). \tag{3}$$

By substituting (2) into (1) and by taking into account the hydrodynamic continuity equation for electrons, upon equating the coefficients of the same power in $(\nabla_r)^k n$, the hierarchy of virtually infinite equations for $\mathbf{g}^k(\mathbf{v})$ is obtained. The first two equations of the resulting set are considered:

$$\frac{e\mathbf{E}}{m_\mathrm{e}} \cdot \nabla_v g^0(\mathbf{v}) = J_\mathrm{el}(g^0) \tag{4}$$

$$\frac{e\mathbf{E}}{m_\mathrm{e}} \cdot \nabla_v \mathbf{g}^1(\mathbf{v}) = J_\mathrm{el}(\mathbf{g}^1) - (\mathbf{v} - \mathbf{W}_\mathrm{d}) g^0(\mathbf{v}), \tag{5}$$

where the binary e–n collision integral for elastic collisions J_el is basically taken in the Boltzmann form (e.g. [29]), assuming a Maxwellian distribution function of temperature T_n for the neutrals. The functions $g^0(\mathbf{v})$ and $\mathbf{g}^1(\mathbf{v})$, as determined from (4) and (5), allow one to define the hydrodynamic parameters, the *electron drift velocity*, $\mathbf{W}_\mathrm{d} (= W_\mathrm{d}\boldsymbol{\kappa})$, which in the case of elastic conservative collisions is given by

$$W_\mathrm{d} = \int \mathbf{v} g^0(\mathbf{v})\, d\mathbf{v}, \tag{6}$$

and the complete *diffusion tensor*, diagonal in the form:

$$\boldsymbol{D} = \boldsymbol{D}_V + \boldsymbol{D}_R = -\int \mathbf{v}\mathbf{g}^1(\mathbf{v})\, d\mathbf{v} = D_\mathrm{L}\boldsymbol{\kappa}\boldsymbol{\kappa} + D_\mathrm{T}(\mathbf{1} - \boldsymbol{\kappa}\boldsymbol{\kappa}), \tag{7}$$

https://doi.org/10.1017/S0022377805004162 Published online by Cambridge University Press

where the transverse D_{T} and longitudinal D_{L} diffusion coefficients have components in velocity and configuration space ($D_{\mathrm{T}} = D_{V\perp} + D_{R\perp}$, $D_{\mathrm{L}} = D_{V\parallel} + D_{R\parallel}$). In solving the system (4) and (5), the standard procedure of expanding $\mathbf{g}^k(\mathbf{v})$ in spherical harmonics in velocity space is applied:

$$\mathbf{g}^k(\mathbf{v}) = \sum_{s=0}^{\infty} \sum_{m=-s}^{s} g^k_{sm}(v) Y_{sm}(\chi, \varphi), \tag{8}$$

where $\cos\chi = -\mathbf{E}\cdot\mathbf{v}/Ev$, and $Y_{sm}(\chi,\varphi) = P_s^m(\cos\chi)\cos m\varphi$, with $P_s^m(\cos\chi)$ denoting the associated Legendre functions. Substituting (8) into equations (4) and (5) and by employing the orthogonality relations for the basis functions a virtually infinite system of *ordinary* differential equations for $g_s^0(v)$ and $\mathbf{g}^1_{sm}(v)$ follows. In practice, to handle these systems, truncation is to be performed at some finite $s = s^*$ for which the convergence of the spherical harmonic expansion is sufficiently rapid to fulfil the imposed accuracy criterion [25]. This leads to the well-known *multiterm solution* of the Boltzmann equation, widely exploited both in electron swarms and in the kinetic theory of low-temperature plasmas, e.g. [16, 18, 19].

For the elastic e–n collision integral J_{el}, appearing on the right-hand side of (4) and (5), the decomposition procedure [27, 29] yields

$$J_{\mathrm{el}}(\mathbf{g}^k_s) = -\mathbf{g}^k_s v N Q^{(s)}(v), \quad s{\neq}0 \quad (k = 0, 1), \tag{9a}$$

for the anisotropic components ($s{\neq}0$), while the Davydov expression [30]

$$J_{\mathrm{el}}(\mathbf{g}^k_0) = \frac{1}{2v^2}\frac{\partial}{\partial v}\left[Nv^3 Q^{(1)}(v)\frac{2m_{\mathrm{e}}}{m_{\mathrm{n}}}\left(\frac{\kappa T_{\mathrm{n}}}{m_{\mathrm{e}}}\frac{\partial}{\partial v} + v\right)\mathbf{g}^k_0\right] \tag{9b}$$

for the zeroth-order ($s = 0$) collision term accounts for the energy loss. Here $Q^{(s)}(v)$, $s{\neq}0$, are the higher-order integral cross-sections, defined as [27]

$$Q^{(s)}(v) = 2\pi \int_0^{\pi} \sigma_{\mathrm{el}}(v,\theta)[1 - P_s(\cos\theta)]\sin\theta\, d\theta \quad (s = 1, 2, \dots), \tag{10}$$

where $\sigma_{\mathrm{el}}(v,\theta)$ is the differential cross-section for elastic e–n collisions, with θ being the scattering angle. In particular $Q^{(1)}(v)$ is the *momentum-transfer* cross-section, $Q^{(1)}(v) \equiv Q_{\mathrm{m}}(v)$, and $Q^{(2)}(v)$ is directly related to the viscosity cross-section $Q_{\mathrm{v}}(v)$ ($Q_{\mathrm{v}} = 2Q^{(2)}/3$) [31]. In the decomposition of $J_{\mathrm{el}}(\mathbf{g}^k_s)$ (9), the transport cross-sections (10) evolve naturally as well-defined quantities, and also determine the corresponding higher-order collision frequencies, of which the *momentum-transfer collision frequency* ν_{m}, is the most well known and used one: $\nu_{\mathrm{m}}(v) = NvQ_{\mathrm{m}}(v)$.

By virtue of expansion (8) the distributions sought, $g_s^0(v)$ and $g^1_{z(x)m\,s}(v)$, become functions of the *scalar* variable, the electron velocity *magnitude* $v = |\mathbf{v}|$. It is both common and convenient at this point to introduce (e.g. [28, 32]) the electron *energy* distribution function(s) (EDF(s)) $f_s^0(\varepsilon)$ related to $g_s^0(v)$ by

$$f_s^0(\varepsilon)\, d\varepsilon = 4\pi v^2 g_s^0(v)\, dv, \quad \varepsilon = \tfrac{1}{2}m_{\mathrm{e}}v^2 \quad (s = 0, 1, \dots). \tag{11}$$

Quite generally, the functions $f^1_{zsm}(\varepsilon)$ and $f^1_{xsm}(\varepsilon)$ are related to the respective $g^1_{zsm}(v)$ and $g^1_{xsm}(v)$ terms by relations analogous to (11).

https://doi.org/10.1017/S0022377805004162 Published online by Cambridge University Press

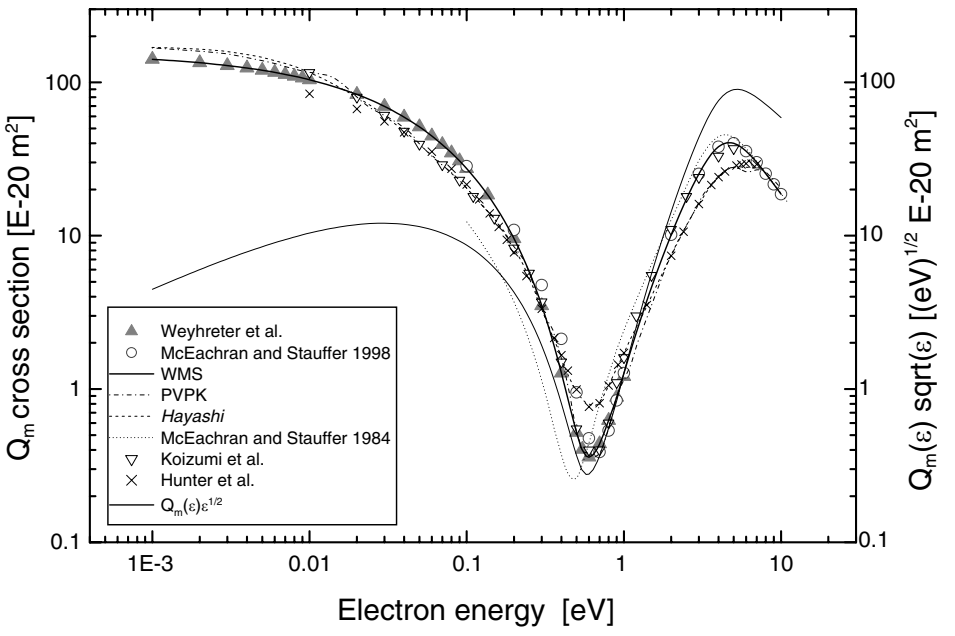


Figure 1. Momentum-transfer Q_{m} cross-section for elastic e–Xe collisions; curves: full bold, presently chosen WMS, interpolating the full triangles, up to 1 eV (Weyhreter et al. [33]) and the hollow circles, at 1 eV and above (McEachran and Stauffer [35]); dot-dashed, Pack et al. [41]; dotted, Hayashi [42]; dotted light, McEachran and Stauffer [36]; points: hollow triangles, Koizumi et al. [43]; crosses, Hunter et al. [51]. *Reduced* momentum-transfer collision frequency $\tilde{\nu}_{\mathrm{m}}(= \sqrt{\frac{1}{2}m_{\mathrm{e}}}\nu_{\mathrm{m}}/N) = \sqrt{\varepsilon}Q_{\mathrm{m}}(\varepsilon)$ for WMS Q_{m}: two-maxima full light curve.

3. Application to xenon

The outlined method is applied to electrons in a weakly ionized xenon plasma. We start at low E/N values, such that the mean electron energy is at least an order of magnitude smaller that the energy coordinate of the RTM in Q_{m} (0.6–0.7 eV) and proceed towards higher values. With the first excitation level for xenon at ≈8.32 eV, we can consider the study, up to a few Td, to be confined to the energy region where the elastic e–Xe collisions are dominant. Presently, we set the boundary of the 'elastic' region slightly above the excitation threshold of xenon (2.87 Td) [20], i.e. at 3 Td, the evaluations at this limit being considered only as provisional.

The set of e–Xe elastic momentum-transfer Q_{m} cross-sections is chosen as follows. For the low-energy region from 0.001 to 1 eV the cross-sections are taken as given by the modified effective range theory (MERT) parameters derived by Weyhreter et al. [33] from their cross-beam measurements of the differential elastic e–Xe cross-section. As the cross-sections [33] apply only to energies below 1 eV (full up triangles in Fig. 1), the theoretical cross-sections due to McEachran and Stauffer [34, 35] are adopted at 1 eV up to 10 eV (hollow circles in Fig. 1). These were derived from the phaseshifts [34, 35] obtained by solving the Dirac equations with relativistic and polarization potentials and exchange included. We choose the cross-sections from these two sources (obviously, independent of swarm experiments), covering jointly the whole energy interval of interest (0.001, 10) eV (full bold curve in Fig. 1) as the *basic* input collision data and denote it as the Weyhreter–McEachran–Stauffer

https://doi.org/10.1017/S0022377805004162 Published online by Cambridge University Press

(WMS) set. The experimental cross-sections of Weyhreter et al. result from scrupulously conducted measurements claiming an energy resolution of 10 meV and an estimated experimental error of below 10%. The 1988 results of Weyhreter et al. [33] show a distinct discrepancy with respect to the early theoretical *non*relativistic results of McEachran and Stauffer [36] (dotted light curve in Fig. 1), but with the relativistic description of the scattering included [34, 35], the theoretical cross-sections thus obtained (hollow circles in Fig. 1), and the experimental ones [33] (full triangles) are brought into much closer agreement. This is understood as the confirmation of the long suspected importance of the electron spin polarization in the elastic scattering of electrons from heavier close-shelled atoms [37]. The original cross-section data, both [33] and [35], refer to phaseshifts, which are highly suitable in the multiterm solving of the Boltzmann equation since all the required higher-order integral cross-sections (10) can easily be restored [38], so that the assumption of isotropic scattering becomes redundant.

The solution for the homogeneous $f_s^0(\varepsilon)$ was originally searched in the three-term approximation ($s = 0, 1, 2$ see Fig. 2, *upper graphs*). However, the large isotropy of EDF ($f_0^0(\varepsilon) \gg f_1^0(\varepsilon) \gg f_2^0(\varepsilon)$) and its convergence property across the RTM proved the two-term approximation for xenon to be adequate when low E/N values and low energies are considered. (Note that the curves in Fig. 2, *upper graphs*, represent f_0^0, $100 \times f_1^0$ and $1000 \times f_2^0$.) Therefore, all the other present calculations are confined to $s = 0, 1$. The physical issues that justify the two-term approximation in the present analysis are:

1. all the stages of the noticeable distortion the EDF undergoes in the low-energy region, due to the RTM (at 0.6–0.7 eV), are accomplished in the E/N range below 1 Td;

2. xenon is a closed-shell atomic gas with the first inelastic process, the first excitation level ($1s_5$) at $\approx$ 8.32 eV. At all the E/N values considered, $E/N <$ 3 Td, the EDF is found to extend below this excitation threshold. This means that the analysis is confined to the energy region where the electrons are undergoing dominantly elastic collisions, with the energy exchange between the electron and the neutral Xe atom being of the order $2m_e/m_n (\approx 8.5 \times 10^{-6})$.

The adequacy of the two-term approximation is also confirmed by the accuracy test proposed by White et al. [25], applied to the EDFs $f_s^0 (s = 0, 1, 2)$:

$$|f_2^0(\varepsilon) P_2(\cos\chi)| \leqslant \delta \left| \sum_{s=0}^{1} f_s^0(\varepsilon) P_s(\cos\chi) \right|, \tag{12}$$

over all energies of interest for the range of E/Ns examined. Irrespective of the specific E/N value from the interval (0.01, 3) Td, the parameter δ introduced by (12), was found to be of the order of 10^{-5} and less, both below 0.05 eV and in the region of the RTM ($\approx$ 0.6–0.7 eV). δ was found to increase towards the high-energy tail of the distribution up to 10^{-4}, where eventually it was found to augment to 10^{-3}.

The adopted 'true' [39] two-term approximation, in the sense of correct treatment of spatial gradients [39, 40], yields the following expressions for the *mean electron energy* $\bar{\varepsilon}$, and the transport coefficients W_d (6), D_T and D_L (7) as functionals of the

https://doi.org/10.1017/S0022377805004162 Published online by Cambridge University Press

energy distributions:

$$\bar{\varepsilon} = \int \varepsilon f_0^0(\varepsilon)\, d\varepsilon, \tag{13}$$

$$W_\mathrm{d} = \frac{1}{3}\sqrt{\frac{2}{m_\mathrm{e}}} \int \sqrt{\varepsilon} f_1^0(\varepsilon)\, d\varepsilon, \tag{14}$$

$$D_\mathrm{T} \approx D_{\varepsilon\perp} = \frac{1}{3}\sqrt{\frac{2}{m_\mathrm{e}}} \int \frac{\sqrt{\varepsilon}}{NQ_m(\varepsilon)} f_0^0(\varepsilon)\, d\varepsilon \tag{15}$$

and

$$D_\mathrm{L} = D_{\varepsilon\parallel} + D_{R\parallel}, \tag{16}$$

where

$$D_{\varepsilon\parallel} = D_{\varepsilon\perp} - \frac{1}{3} W_\mathrm{d} \int \frac{1}{NQ_m(\varepsilon)} f_1^0(\varepsilon)\, d\varepsilon \tag{17}$$

and

$$D_{R\parallel} = \frac{1}{3} eE \sqrt{\frac{2}{m_\mathrm{e}}} \int \frac{\varepsilon}{NQ_m(\varepsilon)} \frac{d}{d\varepsilon}\left[\frac{f_{z00}^1(\varepsilon)}{\sqrt{\varepsilon}}\right] d\varepsilon. \tag{18}$$

The transverse $D_{\varepsilon\perp}$ and longitudinal $D_{\varepsilon\parallel}$ components of the diffusion tensor in the case of spatial homogeneity, i.e. as determined by $f_s^0(\varepsilon)$, differ in an additional contribution of $f_1^0(\varepsilon)$ to $D_{\varepsilon\parallel}$ (17), connected to the drift energy of the electrons. This term is not expected to be determining in atomic gases like xenon, as the drift energy of electrons is distinctly smaller then their thermal energy, but it is retained at present, to preserve the consistency of the two-term approximation [40]. In $D_{R\parallel}$ (18) the spatial inhomogeneity is manifested already with the zeroth-order $f_{z\mathbf{00}}^1(\varepsilon)$ and modifies notably the complete longitudinal diffusion coefficient D_L (16). However, the spatial inhomogeneity of the electron density contributes to $D_{R\perp}$ only in the second-order $f_{x\mathbf{21}}^1(\varepsilon)$ and is, therefore, lost in the two-term approximation ($s = 0, 1$), reducing D_T to the weighted variance of the random velocity $D_{\varepsilon\perp}$ (15). For a distinction to be drawn between D_T and $D_{\varepsilon\perp}$ the three-term approximation is necessary and this would, to our estimates and in agreement with [40], vary the value of D_T within at most 10% of its value according to the applied two-term approximation. Even though the results with imposed error bars of 10% would serve well for a number of plasma applications, they also suit our primary aim of correlating the evaluated transport coefficients to the kinetics of the electron component. Namely, in the decomposition (8), a neat physical meaning is most directly assigned to the lowest EDFs ($s = 0, 1$).

In view of (13)–(18), $f_s^0(\varepsilon)$ and $f_{zs0}^1(\varepsilon)$ ($s = 0, 1$) have been evaluated with the WMS cross-section data, for reduced electric field E/N values extending from 0.01 to 3 Td on the electron energy range from 0.001 to 7 eV (more precisely, $\varepsilon_\mathrm{max}(2\ \mathrm{Td}) = 7$ eV, and specifically at the very limit $\varepsilon_\mathrm{max}(3\ \mathrm{Td}) = 10$ eV) and with the neutrals temperature $T_\mathrm{n} = 300$ K. The applied numerical integral procedure starts at the upper energy limit at which the boundary conditions are given and proceeds to the lower energy limit. At each value of E/N the upper limit ε_max of the energy interval $(0.001, \varepsilon_\mathrm{max})$ is determined by the requirement

$$f_{0,\mathrm{max}}^0(\varepsilon)/f_0^0(\varepsilon_\mathrm{max}) \geqslant 10^5, \tag{19}$$

https://doi.org/10.1017/S0022377805004162 Published online by Cambridge University Press

and the integrations are performed starting from $\varepsilon_{\max}$ up to 0.001 eV in steps of $\Delta\varepsilon$ with $\varepsilon_{\max}/\Delta\varepsilon = 3000$. According to (3) the solution for the homogeneous isotropic distribution function $f_0^0(\varepsilon)$, is normalized to unity. With the aid of the drift velocity $W_{\rm d}$ (14) the inhomogeneous distributions $f_{zs0}^1(\varepsilon)$, $(s = 0, 1)$ are obtained. Subsequently, the transverse (15) and longitudinal (16)–(18) diffusion coefficients, namely, their ratios with mobility, $D_{\rm T}/\mu$, $D_{\rm L}/\mu$ $(\mu = W_{\rm d}/E)$, are evaluated.

Though the WMS $Q_{\rm m}$ are taken as the baseline in the present analysis, in comparing our results with those of other authors, special consideration is given to those pertaining to evaluations with two particular sets of $Q_{\rm m}$s. One set, denoted here as the PVPK $Q_{\rm m}$ is due to Pack et al. [41] (dot-dashed curve in Fig. 1), who have, in addition to their measured $D_{\rm L}/\mu$ values, also reported theoretical values for $W_{\rm d}$, $D_{\rm T}/\mu$ and $D_{\rm L}/\mu$. These they calculated by using the method of Parker and Lowke [13, 14], basically equivalent to the two-term approximation. By repeating the evaluations with their, PVPK, $Q_{\rm m}$ set we have confirmed their theoretical results for the transport coefficients, accomplishing a better than 1% agreement. For the other $Q_{\rm m}$ set we chose the one recommended by Hayashi [42], denoted here as the *Hayashi* $Q_{\rm m}$ set (dotted curve in Fig. 1), with which we parallel the present evaluations. Both *reference* $Q_{\rm m}$ sets have been, over the years, vastly exploited in discharge modelling, mainly at higher E/Ns [44–48], though they differ most remarkably in the region of the RTM. Therefore, we find them highly suitable for testing the sensitivity of the transport coefficients to the depth of the RTM, by using the actual scatter in the respective data, rather than by varying any particular $Q_{\rm m}$ set artificially around the RTM.

4. Results and discussion

4.1. Electron energy distribution function

The characteristic features of the distributions obtained with WMS $Q_{\rm m}$, the homogeneous EDF $f_s^0(\varepsilon, E/N)$ $(s = 0, 1, 2)$ and the inhomogeneous longitudinal EDF $f_{zs0}^1(\varepsilon, E/N)$ $(s = 0, 1)$, are shown in the sequence of *upper* and *lower* graphs of Fig. 2, respectively, for E/N values: (a) 0.04, (b) 0.078, (c) 0.1, (d) 0.12, (e) 0.16, (f) 0.2 and (g) 0.4 Td. As the addressed energy region is the one with predominant elastic e–n collisions, both isotropic functions f_0^0 and f_{z00}^1, presented by full curves in Fig. 2, are considerably larger than their anisotropic corrections (i.e. $f_0^0 \gg f_1^0, (f_2^0)$ and $f_{z00}^1 \gg f_{z10}^1$). Therefore, the latter are presented in Fig. 2 augmented by a factor of 100, dashed (1000, dot-dashed) curves.

In the E/N region examined, (0.01, 3) Td, the dominant isotropic parts of both the homogeneous EDF f_0^0 and the longitudinal EDF f_{z00}^1, undergo most significant modifications on the interval (0.04, 0.4) Td. At $E/N \leqslant 0.04$ Td, $f_0^0(\varepsilon)$ has a pronounced peak below 0.015 eV, while at $E/N \geqslant 0.4$ Td a broad maximum at energies above 1.5 eV is formed. In the intermediate region, shown in Fig. 2, the prominent low-energy peak (see also Fig. 5(a), later in this section), steadily migrates, with increasing E/N, to somewhat higher energies, being notably reduced in height, while an enhancing broad high-energy maximum is formed. Thus, in migrating from low to high energies the electrons exhibit a *double-humped* distribution. The minimum, separating the two humps, shallow at low E/Ns (e.g. Fig. 2(a)), is deepened and drifted to lower energies as the reduced field is increased. The notable distortion of f_0^0 begins to take place at E/Ns for which the mean electron energy $\bar{\varepsilon}$

https://doi.org/10.1017/S0022377805004162 Published online by Cambridge University Press

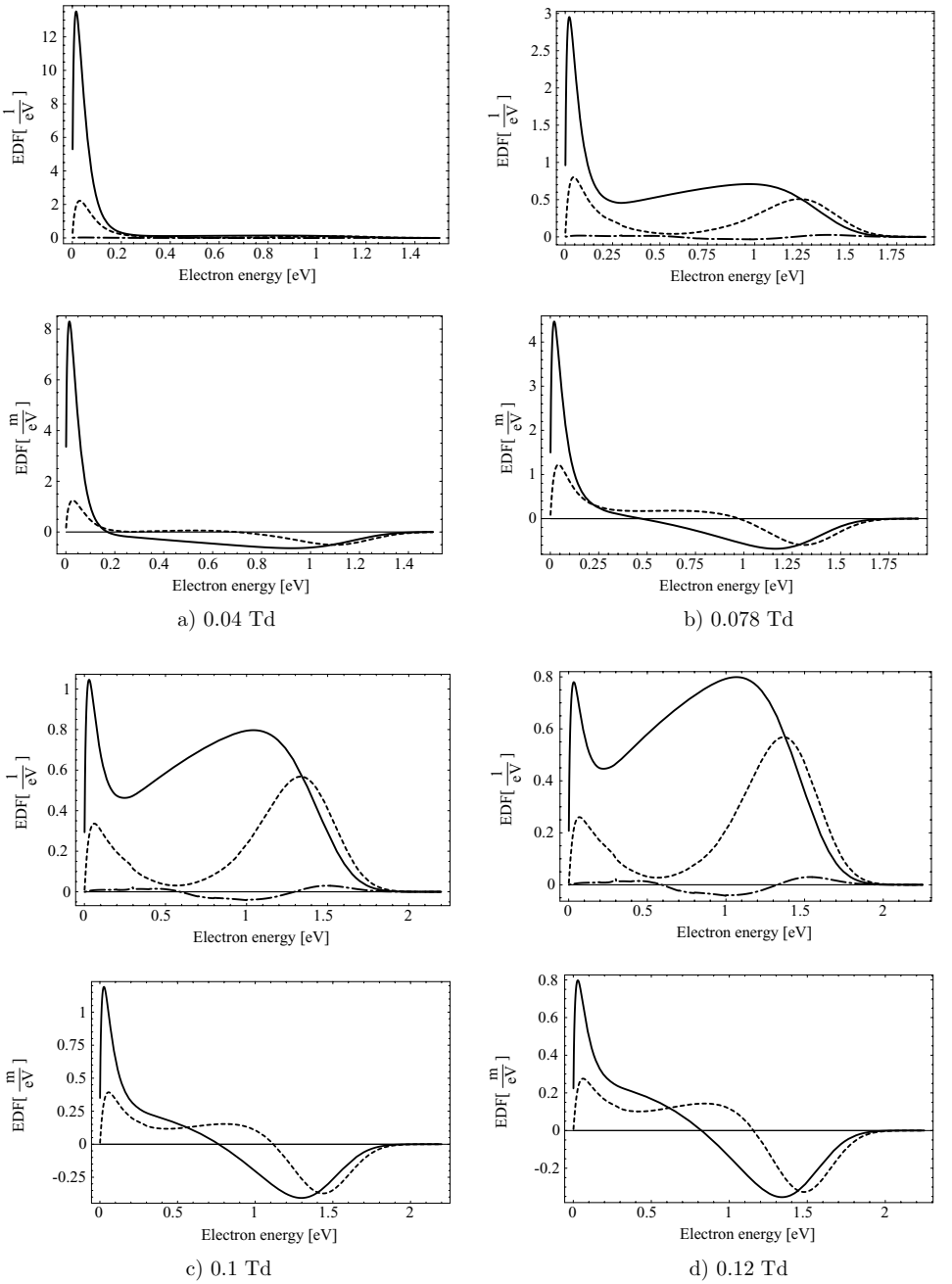
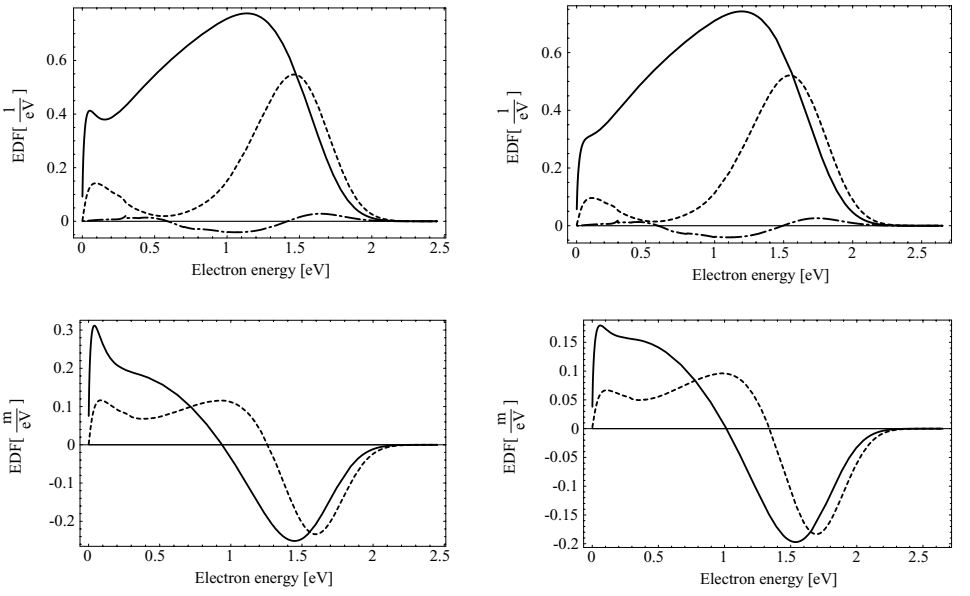
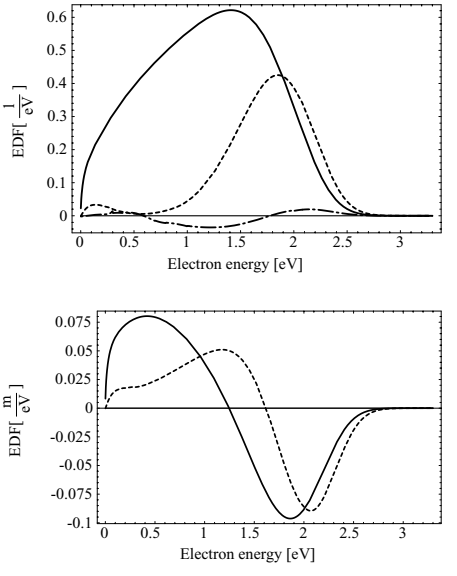


Figure 2. EDF in Xe versus electron energy for E/N: (a) 0.04, (b) 0.078, (c) 0.1, (d) 0.12, (e) 0.16, (f) 0.2 and (g) 0.4 Td with WMS Q_{m} at $T_{\mathrm{n}} = 300$ K. Upper graph: homogeneous EDF $f_s^0(\varepsilon)$; curves: full, $f_0^0(\varepsilon)$; dashed, $100 \times f_1^0(\varepsilon)$; dot-dashed, $1000 \times f_0^2(\varepsilon)$; Lower graph: inhomogeneous longitudinal EDF $f_{zs0}^1(\varepsilon)$; curves: full, $f_{z00}^1(\varepsilon)$, dashed, $100 \times f_{z10}^1(\varepsilon)$.

https://doi.org/10.1017/S0022377805004162 Published online by Cambridge University Press



e) 0.16 Td f) 0.2 Td



g) 0.4 Td

Figure 2. Continued.

has a value close to the energy $\varepsilon_{\mathrm{RTM}}$ of the RTM in Q_{m} cross-section. This is precisely the case shown in Fig. 2(b) where, at 0.078 Td, $\bar{\varepsilon} = 0.607$ eV and $\varepsilon_{\mathrm{RTM}} \approx 0.606$ eV according to the WMS cross-section data. (Similar behaviour of f_0^0 has been found in argon which also displays a salient RTM in Q_{m} (see, e.g., Makabe and Mori [49]).) At 0.12 Td both peaks of f_0^0 are equally populated (Fig. 2(d)), and with further increases of E/N, the second high-energy one is seen to dominate. At 0.4 Td the

https://doi.org/10.1017/S0022377805004162 Published online by Cambridge University Press

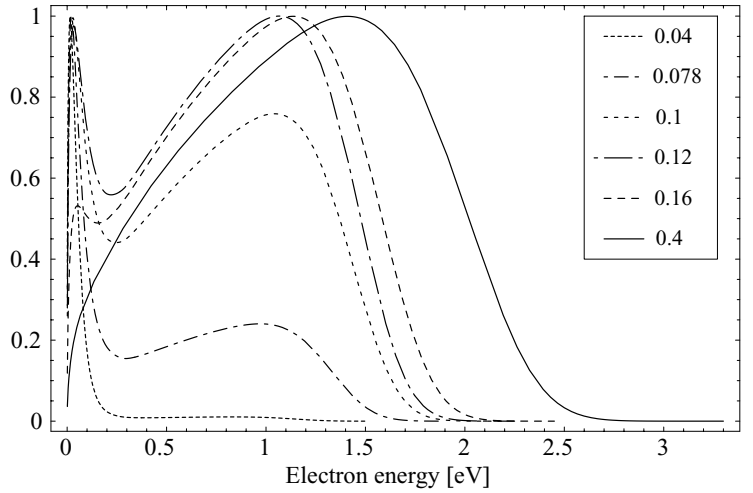


Figure 3. Homogeneous isotropic EDFs $f_0^0(\varepsilon, E/N)$ in Xe with WMS Q_m, at $T_\mathrm{n} = 300$ K normalized to their respective maximum value $f_0^0/f_{0,\max}^0$. Curves: dotted, 0.04 Td, dot-dashed, 0.078 Td; large-dotted, 0.1 Td; dot-large dashed, 0.12 Td; dashed, 0.16 Td and full bold, 0.4 Td.

low-energy hump is completely smoothed out, and the f_0^0 curve with one broad maximum at high energies is formed (Fig. 2(g)). The transition from a one-peaked low-energy f_0^0 to a one-peaked high-energy f_0^0 occurs with the change of E/N over one order of magnitude ((0.04, 0.4) Td), the maxima of the distributions span an energy range of two orders of magnitude (0.015, 1.4) eV, and the mean electron energy increases by a factor of 10 (from 0.13 to 1.2 eV). These remarkable changes in f_0^0, across the E/N range (0.04, 0.4) Td, are also evidenced in Fig. 3, where the distributions $f_0^0(\varepsilon, E/N)$, normalized to their respective maximum value at a given E/N, are jointly displayed.

The anisotropic part of the homogeneous EDF, $f_1^0(\varepsilon, E/N)$ (Fig. 2, *upper graphs*, dashed curves representing $100 \times f_1^0$) though significantly smaller, follows dynamically the behaviour of the double-humped f_0^0. However, there is a distinctive feature of f_1^0: though the low- and high-energy peaks migrate to higher energies with increasing E/N, the minimum between them occurs, for all E/Ns examined, at an almost invariable energy (0.567 ± 0.002 eV), close to the energy coordinate ($\approx$ 0.588 eV) of the minimum in the *momentum-transfer collision frequency* $\nu_\mathrm{m}(\nu_\mathrm{m}(\varepsilon) \propto \sqrt{\varepsilon} Q_\mathrm{m}(\varepsilon))$. (The so-called *reduced* momentum-transfer collision frequency $\tilde{\nu}_\mathrm{m} = \sqrt{\varepsilon} Q_\mathrm{m}(\varepsilon)$ is shown in Fig. 1 by a full *light* curve.) The common location of the minimum in $f_1^0(\varepsilon)$ is conspicuous from Fig. 4, where the $f_1^0(\varepsilon, E/N)$s from Fig. 2 are displayed jointly in real magnitude.

The inhomogeneous, longitudinal isotropic EDF $f_{z00}^1(\varepsilon, E/N)$ (Fig. 2, *lower graphs*, full curves) has values at both sides of the energy axis, in accordance with the normalization condition (3). At lower E/Ns *forward* longitudinal diffusion prevails: low-energy electrons diffuse mainly in the direction of the drift: the population displaying maximal diffusion is only slightly below the low-energy maximum in $f_0^0(\varepsilon)$; scarce higher-energy electrons diffuse in the direction opposite to the drift (e.g. Figs 2(a) and (b)). At each E/N there is a group of electrons that do not experience longitudinal diffusion, i.e. $f_{z00}^1(\varepsilon_0) = 0$ (Fig. 2). Detailed analysis shows

https://doi.org/10.1017/S0022377805004162 Published online by Cambridge University Press

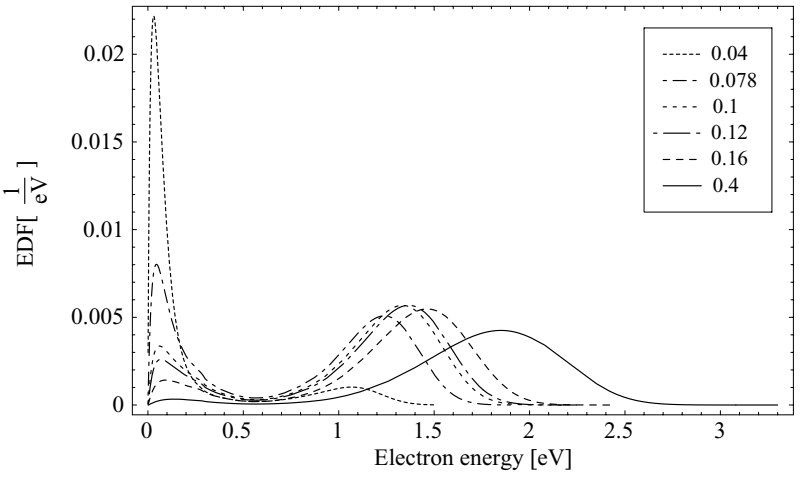


Figure 4. Homogeneous anisotropic EDFs $f_1^0(\varepsilon, E/N)$ in Xe with WMS $Q_{\rm m}$, at $T_{\rm n} = 300$ K. Curves: dotted, 0.04 Td; dot-dashed, 0.078 Td; large-dotted, 0.1 Td; dot-large dashed, 0.12 Td; dashed, 0.16 Td and full bold, 0.4 Td.

that in the region below 0.044 Td and above 0.12 Td these electrons have energies higher than the mean electron energy ($\bar{\varepsilon}$), $\varepsilon_0 > \bar{\varepsilon}$, therefore they produce additional heating of the electron ensemble called *diffusion heating* [28]. In contrast, in the intermediary region (0.044, 0.12) Td, one has $\varepsilon_0 < \bar{\varepsilon}$ and *diffusion cooling* takes place. It is worth noting that at 0.12 Td, with the low- and high-energy peaks of f_0^0 having an equal electron population (Fig. 2(d)), the equality $\varepsilon_0 = \bar{\varepsilon}$ is met, while the population of *non-diffusing* electrons $f_0^0(\varepsilon_0)$ becomes maximal. With further increase of E/N the diffusion in the direction of $\mathbf{W}_{\rm d}$ and in the direction opposite to $\mathbf{W}_{\rm d}$ balance each other: the maximum and minimum of f_{z00}^1 on different sides of the energy axis become almost equal in magnitude. The non-diffusing electrons are highly abundant, their population is close to the overall maximal one (e.g. 0.2, 0.4 Td, Figs 2(f) and (g)) and their energy ε_0, satisfies $\bar{\varepsilon} < \varepsilon_0 < \varepsilon_{\max}$, so that diffusion heating is restored.

Figure 5 illustrates yet another characteristic distinction between f_0^0 and f_{z00}^1 at low E/Ns. Namely, while the low-energy maximum in $f_0^0(\varepsilon, E/N)$ (Fig. 5(a)), is seen to decrease steadily with increasing E/N, the maximum of the longitudinal $f_{z00}^1(\varepsilon, E/N)$ (Fig. 5(b)), does not so. It *ascends* with increasing E/Ns, goes *through a maximum* at ≈0.05 Td (full bold curves in Figs 5(a) and (b)) and then descends with further increases of E/N.

Analogous qualitative behaviour in all the above discussed aspects was observed for the EDFs determined with the two reference cross-section data PVPK $((f_s^0)_{\rm PVPK}, (f_{zs0}^1)_{\rm PVPK})$ and *Hayashi* $((f_s^0)_{\rm Hay}, ((f_{zs0}^1)_{\rm Hay},\ s = 0, 1)$.

4.2. Electron transport coefficients

The mean electron energy $\bar{\varepsilon}$ (13), the electron drift velocity $W_{\rm d}$ (14) and the electron transverse and longitudinal diffusion coefficient to mobility (μ) ratios, ($\mu = W_{\rm d}/E$), namely, $D_{\rm T}/\mu$ and $D_{\rm L}/\mu$, are evaluated with the EDF determined on the basis of WMS $Q_{\rm m}$ cross-sections and presented in Figs 6–8 (full curves) along with the results of other authors. The results of measurements and the Monte Carlo (MC) simulations are shown as discrete points, while the theoretical results of Pack et al. (PVPK) and

https://doi.org/10.1017/S0022377805004162 Published online by Cambridge University Press

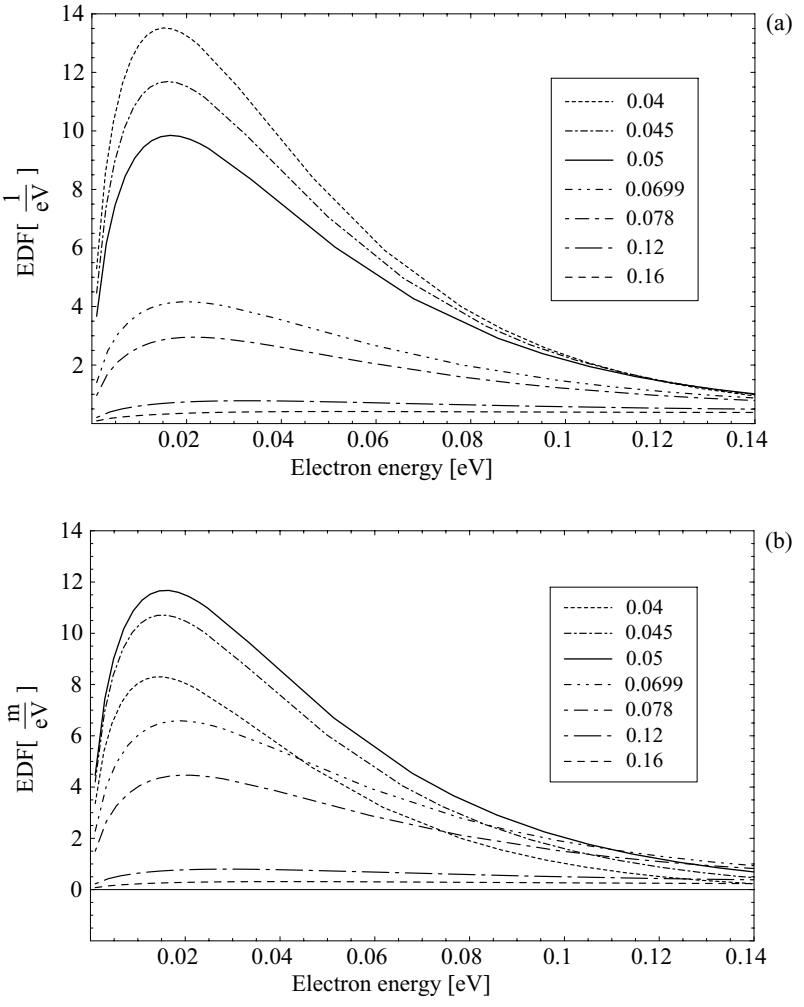


Figure 5. Comparison of the evolution of EDF low-energy maxima with E/N in Xe with WMS Q_{m}, at $T_{\mathrm{n}} = 300$ K: (a) homogeneous $f_0^0(\varepsilon, E/N)$; (b) longitudinal $f_{z00}^1(\varepsilon, E/N)$. Curves: dotted, 0.04 Td; dot-dashed, 0.045 Td; full bold, 0.05 Td; dot-dot-dashed, 0.0699 Td; dot-large dashed, 0.078 Td; dot-largest dashed, 0.12 Td; large dashed, 0.16 Td.

those obtained with *Hayashi* Q_{m} are presented by dot-dashed and dotted curves, respectively. We find it particularly interesting to compare the theoretical results pertaining to the three sets of cross-sections, since the PVPK Q_{m}s (dot-dashed curve in Fig. 1) are quite similar to the WMS (full curve), in the location of the RTM and its depth, while below and above the minimum the WMS cross-sections are higher and in the very low-energy region (below 0.02 eV) lower than those for PVPK. Conversely, the PVPK Q_{m} coincide with the *Hayashi*'s for energies below 0.2 eV and above 2 eV (the dot-dashed and dotted curves overlap there, Fig. 1), while in the intermediary region, enclosing the RTM, the PVPK Q_{m} are, much like the WMS set, substantially lower (by about a factor of 2) than the *Hayashi* values (see Fig. 1). Pack et al. [41] have actually adopted the Hayashi [42] Q_{m}s excluding the region (0.2, 2) eV, where they had adjusted the cross-sections values so as to

https://doi.org/10.1017/S0022377805004162 Published online by Cambridge University Press

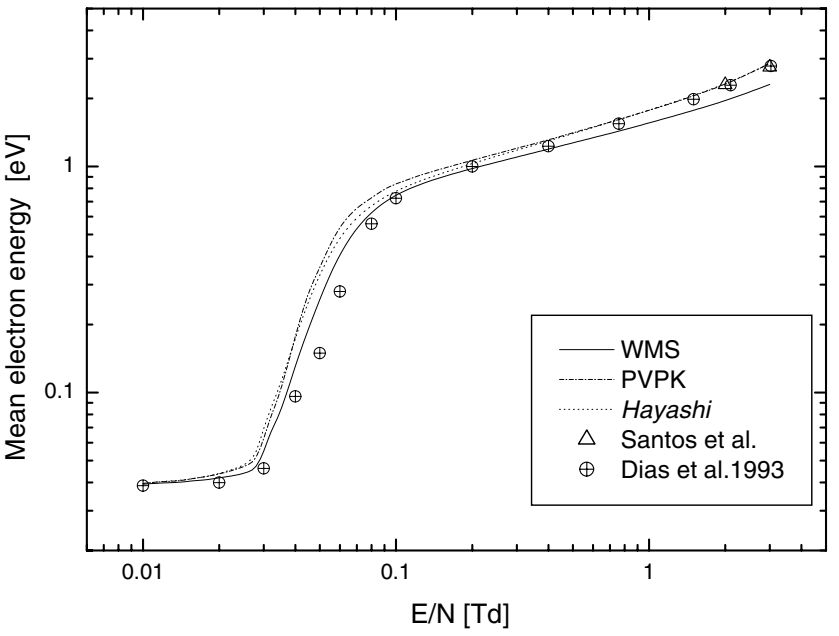


Figure 6. Mean energy, $\bar{\varepsilon}$ versus E/N at $T_n = 300$ K for electrons in Xe. Theoretical values, curves: full, WMS Q_m present; dotted, *Hayashi* Q_m [42]; dot-dashed, PVPK Q_m [41]. Monte Carlo simulation, points: ⊕, Dias et al. [50]; △, Santos et al. [45].

reproduce the D_T/μ values measured and reported by Koizumi et al. [43] (down triangles, ▽ in Figs 8 and 1).

Common to the present results (full curves) for both $\bar{\varepsilon}$ (Fig. 6) and W_d (Fig. 7) is that in the low E/N range they fall between the theoretical PVPK values (dot-dashed curve) and the results of the 3D MC simulation of Dias et al. [50] (⊕ for $\bar{\varepsilon}$ in Fig. 6 and + for W_d in Fig. 7), while at higher E/Ns they remain the lowest of the compared data sets. The PVPK (dot-dashed) and *Hayashi* (dotted) mean energy curves in Fig. 6 appear superimposed for E/N values below 0.025 Td and above 0.4 Td, which delimit the low- and high-energy ranges where the respective cross-sections coincide. In the intermediate E/N range comprising the RTM, the discrepancy in $\bar{\varepsilon}$ is kept within 10%, though the PVPK and *Hayashi* Q_ms differ by a factor of 2 there (Fig. 1). Conversely, the WMS and PVPK cross-sections that agree fairly well across the RTM (Fig. 1), but otherwise differ by some 25–35%, induce the same order of deviations in the respective $\bar{\varepsilon}$-values (full and dot-dashed curves in Fig. 6). The depleted electron population at energies around the RTM (Fig. 2) causes the contribution of this energy region to $\bar{\varepsilon}$ to be minor.

As far as the electron drift velocity is concerned, the dot-dashed PVPK and dotted *Hayashi* curves in Fig. 7 with the scatter of values below 2%, practically overlap up to 0.1 Td and above 1 Td (see also Fig. 9). Large deviations in Q_m across the RTM are even less influential in W_d than in $\bar{\varepsilon}$. The insensitivity of W_d to the RTM is confirmed further by the experimental values of Hunter et al. [51] (squares, □ in Fig. 7). The Q_ms (crosses, ×, in Fig. 1) that Hunter et al. unfolded from their W_d measurements agree very well over the RTM, with *Hayashi* Q_ms, and consequently they disagree notably with the PVPK Q_ms, a fact completely masked

https://doi.org/10.1017/S0022377805004162 Published online by Cambridge University Press

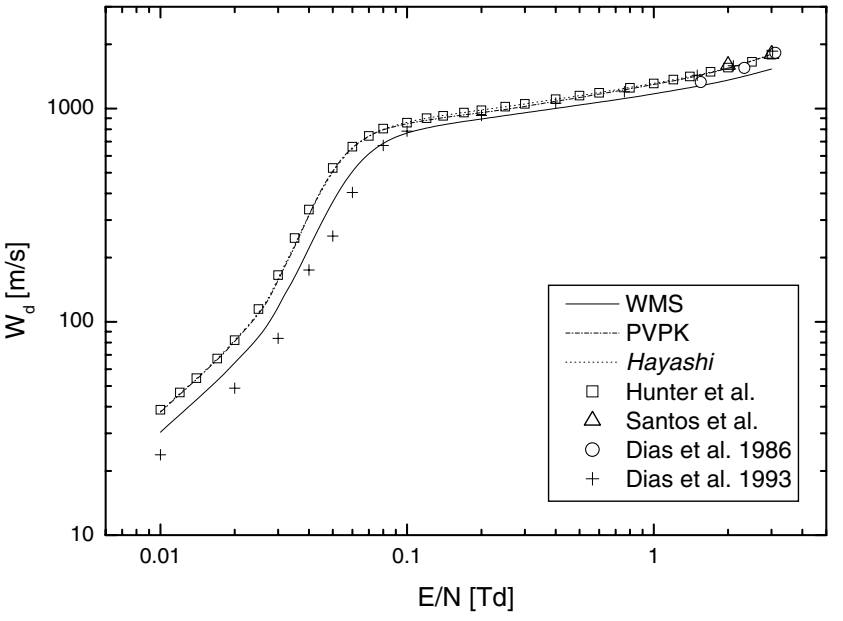


Figure 7. Drift velocity W_d versus E/N at $T_n = 300$ K for electrons in Xe. Theoretical values, curves: full, WMS Q_m present; dotted, *Hayashi* Q_m [42]; dot-dashed, PVPK Q_m [41]. Experimental values □, Hunter et al. [51]. Monte Carlo simulations, points: ○, Dias et al. [52]; +, Dias et al. [50]; △, Santos et al. [45].

by the very good agreement among the respective W_d values. However, WMS Q_ms, in the region *below* and *above* the RTM distinctly larger both than the PVPK and the *Hayashi* set, bring about lower drift velocities (full curve). The extent to which $\bar{\varepsilon}$ and W_d are insensitive to the cross-section data over the RTM is also evident from comparison with the MC results [45,50,52]. The results of Santos et al. [45] indicated by △ and those of Dias et al. [50] shown by ⊕ in Fig. 6, and by + in Fig. 7, were obtained by using *Hayashi* [42] cross-sections in the higher-energy region; however, over RTM the relativistic cross-sections of Stauffer et al. [53], distinctly lower than the corresponding *Hayashi* [42] ones, were applied. Nevertheless, for E/Ns above 0.1 Td, the agreement between the MC and *Hayashi* (and PVPK) values is remarkable, when either the mean energy or the drift velocity is concerned. The relativistic integral elastic cross-sections Q_t of Sin Fai Lam [54] were used over the complete energy range in the MC results above 1 Td [52], represented by ○ in Fig. 7. Higher values of relativistic cross-sections [54], with respect to the *Hayashi* ones, in the region above 1 eV, lower the W_d values bringing them closer to the present WMS results. For W_d, this confirms both the low sensitivity to the RTM, and the high sensitivity to the cross-sections at energies above the RTM.

As the two-term representation of the EDF $f_1^0(\varepsilon)$ indicates

$$f_1^0(\varepsilon) = \frac{eE}{NQ_m(\varepsilon)}\left[\frac{f_0^0(\varepsilon)}{2\varepsilon} - \frac{df_0^0(\varepsilon)}{d\varepsilon}\right], \tag{20}$$

the main contribution to W_d comes from the energy region above 1 eV where f_0^0, descends at the largest (negative) rate (Fig. 2), giving rise to the second maximum in f_1^0. The depth of the RTM has almost no consequence on the W_d characteristic;

https://doi.org/10.1017/S0022377805004162 Published online by Cambridge University Press

below the RTM the drift velocity is susceptible to the energetically poor region below 0.1 eV, which is manifested only at very low E/Ns; above the RTM W_d is most sensitive to energies above 1 eV.

In terms of f_1^0 itself, the lack of sensitivity of the drift velocity W_d to the depth of the RTM in Q_m can be explained by the general behaviour of f_1^0 (Fig. 4) which has the two maxima separated by a broad minimum at an energy practically independent of E/N and quite close to the energy coordinate of the RTM in ν_m. Regardless of the E/N value in question, the contribution of the electrons with energies around the ε_{RTM} to the drift velocity is effectively negligible.

The presently evaluated D_T/μ (full upper curve in Fig. 8), are in good agreement with the theoretical PVPK values (dot-dashed upper curve), which in turn (as expected) reproduce remarkably well the experimental values of Koizumi et al. (down triangles, $\triangledown$) in the interval susceptible to D_T/μ measurements [43]. Conversely, there is poor agreement between these sets on one hand and the *Hayashi* (dotted curve) and Suzuki ($\diamondsuit$) D_T/μ values on the other. With the exception of very low E/Ns, the D_T/μ MC results of Dias et al. [50] and of Santos et al. [45] ($+$ and Δ, respectively, in Fig. 8) fall between the present evaluations and the experimental values of Suzuki et al. [7]. At E/Ns above 1 Td they distinctly tend to the *Hayashi* values (and so do the corresponding D_L/μ values) confirming the validity of the presently applied approximation, as well as the determining choice of cross-section data, at higher energies, independently of the evaluation technique used.

The most striking information in Fig. 8, as far as D_T/μ is concerned, is that, quite contrary to the case of W_d, *Hayashi* and PVPK Q_ms (that differ by a factor of 2 over the RTM, but otherwise coincide), lead to substantially different D_T/μ values, practically over the whole E/N range above 0.03 Td. The great sensitivity of D_T/μ to the RTM is indeed common to all heavier inert gases and has been extensively used in swarm experiments, e.g. [10,43]. Electrons with energies around the ε_{RTM} and above, up to the maximum in f_0^0, contribute to D_T most. The lower the RTM in Q_m is, the lower the elastic losses, and the higher the mean free time for momentum-transfer, i.e. the higher D_T and D_T/μ are. This is most clearly observed in Fig. 8 when looking at a given E/N (above 0.06 Td), the vertical sequence of D_T/μ values: the highest being the WMS values that correspond to the lowest RTM in Q_m ($(Q_m)_{RTM}^{WMS} = 0.359\times10^{-20}$ m^2) and the lowest being the Suzuki et al. values [7] corresponding to the highest RTM in Q_m ($(Q_m)_{RTM}^{Suzuki} = 0.9 \times 10^{-20}$ m^2). The RTM value of Q_m, if evaluated with the cross-section data [53], used in the simulations of Dias et al. and Santos et al., would fall between the RTM of the PVPK and the *Hayashi* momentum-transfer cross-section, as anticipated by the respective D_T/μ values ($+, \triangle$) shown in Fig. 8.

The present longitudinal diffusion coefficient to mobility ratio D_L/μ (lower full curve, Fig. 8), and the theoretical PVPK set (lower dot-dashed curve) show larger scatter then the respective D_T/μs. While both D_L/μ sets (WMS and PVPK) show discrepancies with respect to the *experimental* PVPK D_L/μ values (squares, $\square$), the present WMS D_L/μ values conform to the MC results ($\times$) best. The *Hayashi* and theoretical PVPK D_L/μs (dotted and dot-dashed lower curves, respectively) apart from being in good overall agreement, apparently confirm the experimental values of Suzuki et al. [7] ($\diamondsuit$), especially above 0.1 Td.

For E/N values below 0.02 Td all the data in Fig. 8 converge, the ratio D_L/D_T tends to unity, while both D_L/μ and D_T/μ tend to the Einstein limit $\kappa T_n/e$, where κ

https://doi.org/10.1017/S0022377805004162 Published online by Cambridge University Press

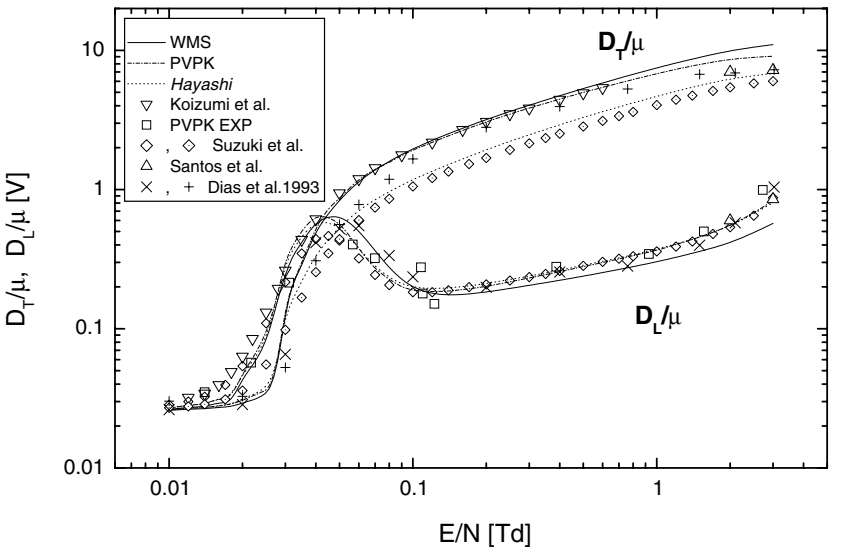


Figure 8. D_T/μ and D_L/μ versus E/N at $T_n = 300$ K for electrons in Xe. Theoretical values, curves: full, WMS Q_m present; dotted, *Hayashi* Q_m [42]; dot-dashed, PVPK Q_m [41]. Points; experimental values: ▽, Koizumi et al. [43]; □, Pack et al. [41]; ◇, Suzuki et al. [7]; Monte Carlo simulations: + and ×, Dias et al. [50]; △, Santos et al. [45].

is the Boltzmann constant (e.g. [23]). At this very low E/N-limit electron diffusion is governed primarily by the thermal motion of the gas neutrals rather than by the electric field.

According to all the (D_T/μ, D_L/μ) sets presented (Fig. 8) the well-known anisotropy in diffusion is distinctly displayed: at lower E/N values $D_L/\mu > D_T/\mu$, while at higher E/Ns one has $D_L/\mu < D_T/\mu$. The only exception are the MC results [50] at the two lowest E/Ns considered (0.01 and 0.02 Td) where one has $D_T/\mu > D_L/\mu$ (+ and ×, respectively, in Fig. 8) and is, to a certain extent, indicative of the known inefficiency of the MC method operating at very low E/Ns and low energies. The coefficient D_L/μ goes through the maximum for the E/N value either slightly higher (WMS, Dias et al. [50]) or slightly lower (PVPK, *Hayashi*, Suzuki et al. [7]) than the $(E/N)_D$ for which $D_L = D_T$ with the height of the D_L/μ maximum being governed by the depth of the Q_m RTM. The lower the minimum in Q_m is, the higher the maximum in D_L/μ. According to the presently adopted WMS Q_m set, as well as to all the data we have compared with, both the equality $D_L = D_T$ and the maximum in D_L/μ are reached on the interval (0.04, 0.05) Td. (The only exception is the D_L/μ maximum, according to the MC results [50], estimated to take place at 0.06 Td, though the step in the variation of the E/N parameter within the MC method was rather large to set this unambiguously.)

In xenon the E/N range (0.04, 0.05) Td corresponds to the region of momentum-transfer collision frequencies with the largest decreasing rate $d\nu_m/d\bar{\varepsilon}$; it is also the region where the rate of increase of the ratio D_T/μ, as well as the rate of increase of the drift velocity W_d and the mean electron energy $\bar{\varepsilon}$ (Figs 6–8) per reduced electric field is the largest. In contrast, on the same interval, (0.04, 0.05) Td, D_L/μ attains its maximum, the highest of the maxima in $f^1_{z00}(\varepsilon, E/N)$ is reached there

https://doi.org/10.1017/S0022377805004162 Published online by Cambridge University Press

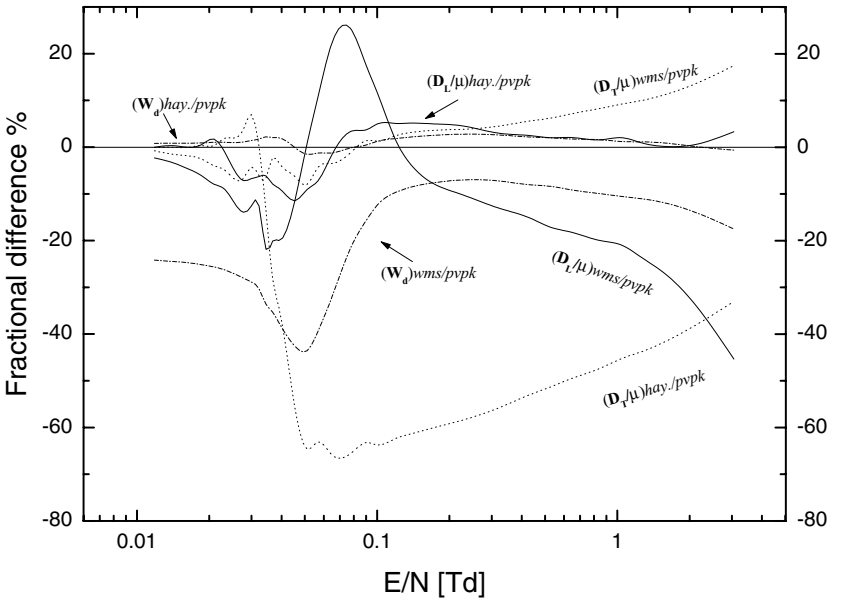


Figure 9. Fractional difference in $W_{\rm d}$, $D_{\rm T}/\mu$ and $D_{\rm L}/\mu$ versus E/N, as evaluated with WMS present, *Hayashi* [42] and PVPK $Q_{\rm m}$ [41] sets. Curves: full, $D_{\rm L}/\mu$; dotted, $D_{\rm T}/\mu$; dot-dashed, $W_{\rm d}$.

(Fig. 5(b)), while the population of electrons having no longitudinal diffusion goes through its minimum, according to the WMS as well as to both PVPK and *Hayashi* $Q_{\rm m}$s. In the subsequent region up to 0.16 Td, which corresponds to the reshaping of $f_0^0(\varepsilon, E/N)$ across the RTM through the double-humped distribution (Fig. 2), $D_{\rm L}/\mu$ has the characteristic descent – a manifestation of diffusion cooling. In this process the population of the non-diffusing electrons increases, tending to approach the population at the developing second maximum in f_0^0. The shallow minimum in $D_{\rm L}/\mu$ (Fig. 8), corresponding to the maximum in the population of non-diffusing electrons, is apparently maintained until the second high-energy maximum in f_0^0 is clearly established as the dominant one. From there onwards, diffusion heating takes place again. As the EDF with one single maximum is formed, (0.2, 0.4) Td, the population of non-diffusing electrons drops and $D_{\rm L}/\mu$ increases again, the increase being slower as forward and backward diffusion slowly balance out, and $Q_{\rm m}$ begins to increase after the RTM.

Finally, the proper extent to which the values of the transport coefficients obtained with *reference* cross-section data mutually agree/disagree over the examined E/N region can be estimated from Fig. 9, where the fractional difference in their respective values is presented as a function of E/N. We define the fractional difference, for instance, for $W_{\rm d}$, when comparing its values pertaining to the WMS and to the PVPK cross-section sets as

$$(W_{\rm d})_{\rm WMS/PVPK} = \frac{(W_{\rm d})_{\rm WMS} - (W_{\rm d})_{\rm PVPK}}{(W_{\rm d})_{\rm WMS}}, \tag{21}$$

and in an analogous manner $(W_{\rm d})_{\rm Hay/PVPK}$, and similarly for $D_{\rm T}/\mu$ and $D_{\rm L}/\mu$.

The dot-dashed $(W_{\rm d})_{\rm Hay/PVPK}$ curve in Fig. 9 indicates that the overlapping of the $W_{\rm d}$ curves, below 0.1 Td and above 1 Td in Fig. 7, corresponds to the agreement

https://doi.org/10.1017/S0022377805004162 Published online by Cambridge University Press

between the respective W_d values within 2%, while it rests within 3% over the complete E/N region examined. However, discrepancies in WMS and PVPK W_d values are as high as 40% (dot-dashed $(W_d)_{WMS/PVPK}$ curve), WMS W_ds being systematically lower: a consequence of higher Q_ms (≈30%) both below and above the RTM.

As already conveyed by Fig. 8, the *Hayashi* and PVPK values (concerning D_T/μ) differ considerably, which amounts up to 65% at the RTM (dotted $(D_T/\mu)_{Hay/PVPK}$ curve in Fig. 9). The disagreement, abruptly reached at the RTM, is reduced to some 35% at the largest E/Ns considered, mainly due to the equality of Q_ms above 2 eV and the similarity in the pertaining $(f_0^0)_{Hay}$ and $(f_0^0)_{PVPK}$ at E/Ns above 0.4 Td, for which the one-maximum f_0^0 is accomplished. The good agreement between WMS and PVPK D_T/μ amounts to 10% up to 1 Td (dotted $(D_T/\mu)_{WMS/PVPK}$ curve). However, Q_m values, differing by more than 30% at energies above 2 eV (Fig. 1), increase the fractional difference to some 20% at the high-E/N limit. The D_L/μ values according to *Hayashi* and PVPK are in satisfactory agreement (Fig. 9, full $(D_L/\mu)_{Hay/PVPK}$ curve). The largest deviations, near 10%, are around the D_L/μ and $f_{00z}^1(E/N)$ maxima, and are almost twice as small at the reshaping of the EDF, around the shallow D_L/μ minimum. The large discrepancy in the depth of the RTM in Q_m (Fig. 1: $(Q_m)_{RTM}^{Hay} = 0.785 \times 10^{-20}$ m^2, $(Q_m)_{RTM}^{PVPK} = 0.360 \times 10^{-20}$ m^2) does not affect diffusion along the electric field at higher E/Ns. However, scatter among the WMS and PVPK D_L/μs amounts to 25% in the RTM region. The respective minimal Q_m values coincide fairly well there ($(Q_m)_{RTM}^{WMS} = 0.359 \times 10^{-20}$ m^2), consequently the maxima in D_L/μ are almost equal in height (Fig. 8), but are displaced in their E/N coordinates due to the different energy coordinates of the RTM ($\varepsilon_{RTM}^{WMS} = 0.606$ eV, $\varepsilon_{RTM}^{PVPK} = 0.650$ eV) (Fig. 1). Deviations are again increased at higher E/Ns, revealing the increasing discrepancy between the Q_m sets after the RTM: WMS Q_ms higher than PVPK Q_ms deplete more significantly the electron population at the energy tail, thus yielding respectively lower D_L/μ values.

5. Concluding remarks

The patterns of the homogeneous and inhomogeneous longitudinal EDFs, as obtained from the solution of the Boltzmann equation in the hydrodynamic regime, are correlated to the behaviour of the standard electron transport coefficients in xenon weakly ionized plasma, over the energy and E/N domains enclosing the RTM in elastic e–Xe scattering. The set of cross-sections due to Weyhreter and McEachran and Stauffer (WMS Q_m) [33, 35] is taken as the baseline of the study. The E/N region (0.01, 3) Td is analysed, within which the notable distortion of the EDFs is found to be confined to the interval (0.04, 0.4) Td. Clearly enough, to provide evidence for these changes a fine mesh of E/N values is required.

The results can be summarized as follows.

• Occurrence of the transition of the homogeneous EDF from the single low-energy maximum f_0^0 at low E/Ns, through the double-humped f_0^0, to a single high-energy maximum f_0^0 at higher E/Ns. The distortion of f_0^0 becomes apparent at the E/N value at which the mean electron energy $\bar{\varepsilon}$ corresponds closely to the value of the energy coordinate of the RTM in Q_m ($\bar{\varepsilon} = \varepsilon_{RTM}$).

• Similarly, f_1^0 exhibits a double maximum; however, this is also noticeable at higher E/Ns at which the low-energy maximum in f_0^0 is completely smoothed out.

https://doi.org/10.1017/S0022377805004162 Published online by Cambridge University Press

The minimum in f_1^0 is settled at an energy close to the energy coordinate of the minimum in ν_m irrespective of the E/N examined.

• The inhomogeneous longitudinal f_{z00}^1 has values on both sides of the energy axis. The low-energy maximum, prominent at low E/Ns, migrates to higher energies with increasing E/N, but in contrast to f_0^0 does not steadily decrease. It increases for low E/Ns, goes through the maximum at ≈ 0.05 Td and decreases with further increase of E/N.

• The insensitivity of the drift velocity W_d to the RTM can be explained by the structure of the anisotropic f_1^0. The anisotropy is the largest in the energy region after the (high-energy) maximum and near the tail of the f_0^0, where the *descending* rate (slope) $|df_0^0/d\varepsilon|$ is the largest. As the form of f_1^0 (two E/N-dependent maxima separated by a *fixed* minimum located close to the minimum in ν_m) clearly suggests, the contribution of the electrons 'trapped' at the RTM to the drift velocity is effectively negligible, irrespective of the E/N considered.

• In the low-E/N range where both f_0^0 and f_{z00}^1 have pronounced low-energy maxima, the two coefficients D_T/μ and D_L/μ ($D_T/\mu < D_L/\mu$) have analogous ascending behaviour. However, by increasing E/N the restructuring of the EDFs begins to take place. D_L/μ goes through the maximum at the E/N at which the ascending maximum in $f_{z00}^1(E/N)$ reaches the highest value. With increasing E/N further, the maximum in f_{z00}^1 starts to descend and so does D_L/μ. Diffusion in the direction opposite to $\mathbf{W}_d$ becomes more pronounced and the group of non-diffusing electrons with energy $\varepsilon_0 < \bar{\varepsilon}$, produces diffusion cooling. The subsequent shallow minimum in D_L/μ is achieved when the high-energy maximum in f_0^0 becomes dominant, diffusion in the direction of $\mathbf{W}_d$ and opposite to $\mathbf{W}_d$ balance each other $|(f_{z00}^1)_{max}| \approx |(f_{z00}^1)_{min}|$ and diffusion heating is restored $\varepsilon_0 > \bar{\varepsilon}$. From there on, D_L/μ increases again with increasing E/N. The characteristic decrease of D_L/μ is a direct consequence of diffusion cooling and of the double-humped distribution $f_0^0(\varepsilon, E/N)$, both of which are induced by the RTM.

It has been demonstrated that the influence of the RTM on electron transport in xenon is strongly dominated by the behaviour of the EDFs. Maxwellian and bi-Maxwellian EDFs that ignore the prominent $\nu_m(\varepsilon)$ energy dependence, generally lead to overestimated electron transport coefficients, e.g. [48], and are thus not suitable for modelling heavy inert-gas discharges at low mean energies.

It can be inferred that in unfolding cross-sections from swarm data by the Boltzmann equation method, in the range of E/Ns from the values where $\bar{\varepsilon} \approx \varepsilon_{RTM}$ to the values close to the shallow minimum in D_L/μ, $\bar{\varepsilon} \approx \varepsilon_0$, the modelling of the electron EDF f_0^0 in xenon should allow for two maxima. The present analysis indicates that this could lead to an improved convergence of the electron Q_ms, which have a considerable spread in recent literature, when xenon, as well as other heavier inert gases and their RTM regions are concerned.

Adding a heavy inert gas to a buffer gas of the discharge enhances the mean electron energy [8]. At low E/Ns diffusion heating/cooling could be used, as a mechanism of controlling the energy of the electron swarm in xenon mixtures.

Relationships between the EDFs and the transport parameters similar to those for xenon are expected to be found in other heavy inert gases and also in molecular gases that display the RTM. However, as far as krypton, argon or methane are concerned, the relevant range of electron energies and E/Ns is to be shifted to values lower than those in xenon [49, 55].

https://doi.org/10.1017/S0022377805004162 Published online by Cambridge University Press

Acknowledgements

The author wishes to thank Professor C. A. N. Conde and Dr T. H. V. T. Dias from the University of Coimbra, and Professor M. Suzuki from Akita University, for kindly providing their electron transport results for xenon in tabular form.

References

[1] Anderson, C. A. and Graham, W. G. 1995 *Plasma Sources Sci. Technol.* **4**, 561.
[2] Kimura, T., Lichtenberg, A. J. and Lieberman, M. A. 2001 *Plasma Sources Sci. Technol.* **10**, 430.
[3] White, R. D., Robson, R. E. and Ness, K. F. 2001 *Computer Phys. Commun.* **142**, 349.
[4] Pinheiro, M. J. and Loureiro, J. 2002 *J. Phys.* D **35**, 1.
[5] Gortchakov, S., Lange, H. and Uhrlandt, D. 2003 *J. Appl. Phys.* **93**, 9508.
[6] McEachran, R. P. and Elford, M. T. 2003 *J. Phys.* B **36**, 427.
[7] Suzuki, M., Taniguchi, T., Yoshimura, N. and Tagashira, H. 1992 *J. Phys.* D **25**, 50; Private communication 2001.
[8] Nagpal, R. and Garscadden, A. 1994 *Phys. Rev. Lett.* **73**, 1598.
[9] Schmidt, B., Berkhan, K., Götz, B. and Müller, M. 1994 *Phys. Scr.* **53**, 30.
[10] Atrazhev, V. M., Chernysheva, I. V. and Doke, T. 2002 *Jpn. J. Appl. Phys.* **41**, 1572.
[11] Frost, L. S. and Phelps, A. V. 1964 *Phys. Rev.* **136**, A1538.
[12] Skullerud, H. R. 1969 *J. Phys.* B **2**, 696.
[13] Parker, J. H. and Lowke, J. J. 1969 *Phys. Rev.* **181**, 290.
[14] Lowke, J. J. and Parker, J. H. 1969 *Phys. Rev.* **181**, 302.
[15] Date, H., Ishimaru, Y. and Shimozuma, M. 2003 *Nucl. Instrum. Meth. Phys. Res.* B **207**, 373.
[16] Pitchford, L. C., O'Neil, S. V. and Rumble, J. R. Jr. 1981 *Phys. Rev.* A **23**, 294.
[17] Longo, S. 2000 *Plasma Sources Sci. Technol.* **9**, 468.
[18] Loffhagen, D., Sigeneger, F. and Winkler, R. 2002 *J. Phys.* D **35**, 1768.
[19] Loffhagen, D. and Winkler, R. 1996 *Plasma Sources Sci. Technol.* **5**, 710.
[20] Dias, T. H. T. V., Santos, F. P., Ranchinchas, P. J. B. M., Borges, F. I. G. M. and Stauffer, A. D. 1999 *J. Appl. Phys.* **85**, 6303.
[21] Uchida, S., Sugawara, H., Sakai, Y., Watanabe, T. and Byoung-Hee Hong 2000 *J. Phys.* D **33**, 62.
[22] Boeuf, J. P. 2003 *J. Phys.* D **36**, R53.
[23] Huxley, L. G. H. and Crompton, R. W. 1974 *The Diffusion and Drift of Electrons in Gases*. New York: Wiley.
[24] Lin, S. L., Robson, R. E. and Mason, E. A., 1979 *J. Chem. Phys.* **71**, 3483.
[25] White, R. D., Robson, R. E., Schmidt, B. and Morrison, M. A. 2003 *J. Phys.* D **36**, 3125.
[26] Kumar, K. and Robson, R. E. 1973 *Aust. J. Phys.* **26**, 157.
[27] Kumar, K., Skullerud, H. R. and Robson, R. E. 1980 *Aust. J. Phys.* **33**, 343.
[28] Makabe, T. and Mori, T. 1984 *J. Phys.* D **17**, 699.
[29] Shkarofsky, I. P., Johnston, T. W. and Bachynski, M. P. 1966 *The Particle Kinetics of Plasmas*. Reading, MA: Addison-Wesley.
[30] Davydov, B. I. 1937 *Zhurn. Eks. Teor. Fiz.* **7**, 1069.
[31] Žigman, V. 1999 *Eur. Phys. J.* D **7**, 11.
[32] Lieberman, M. A. and Lichtenberg, A. J. 1994 *Principles of Plasma Discharges and Materials Processing*. New York: Wiley.
[33] Weyhreter, M., Barzick, B., Mann, A. and Linder, F. 1988 *Z. Phys.* D **7**, 333.
[34] McEachran, R. P. and Stauffer, A. D. 1987 *J. Phys.* B **20**, 3483.

https://doi.org/10.1017/S0022377805004162 Published online by Cambridge University Press

[35] McEachran, R. P. and Stauffer, A. D. 1998 Private communication.
[36] McEachran, R. P. and Stauffer, A. D. 1984 *J. Phys.* B **17**, 2507.
[37] Kessler, J. 1996 *Can. J. Phys.* **74**, 863.
[38] Žigman, V. 1995 *J. Phys.* B **28**, L239.
[39] Segur, P. and Bordage, M. C. 1987 *ICPIG XVIII Contrib. Papers* **1**, 156 Swansea.
[40] Brennan, M. J. and Ness, K. F. 1992 *Nuovo Cimento* **14D**, 933.
[41] Pack, J. L., Voshall, R. E., Phelps, A. V. and Kline, L. E. 1992 *J. Appl. Phys.* **71**, 5363; AIP document no PAPS JAPIA-71-5363-8.
[42] Hayashi, M. 1983 *J. Phys.* D **16**, 581.
[43] Koizumi, T., Shirakawa, E. and Ogawa, I. 1986 *J. Phys.* B **19**, 2331.
[44] Puech, V. and Mizzi, S. 1991 *J. Phys.* D **24**, 1974.
[45] Santos, F. P., Dias, T. H. V. T., Stauffer, A. D. and Conde, C. A. N. 1994 *J. Phys.* D **27**, 42.
[46] Meunier, J., Belenguer, Ph and Boeuf, J. P. 1995 *J. Appl. Phys.* **78**, 731.
[47] Kochetov, I. V., Napartovich, A. P., Ye, C. and Lo, D. 1998 *J. Appl. Phys.* **84**, 1863.
[48] Carman, R. J. and Mildren, R. P. 2000 *J. Phys.* D **33**, L99.
[49] Makabe, T. and Mori, T. 1982 *J. Phys.* D **15**, 1395.
[50] Dias, T. H. V. T., Santos, F. P., Stauffer, A. D. and Conde, C. A. N. 1993 *Phys. Rev.* A **48**, 2887; Private communication 2004.
[51] Hunter, S. R., Carter, J. G. and Chistophorou, L. G. 1988 *Phys. Rev.* A **38**, 5539.
[52] Dias, T. H. V. T., Stauffer, A. D. and Conde, C. A. N. 1986 *J. Phys.* D **19**, 527.
[53] Stauffer, A. D., Dias, T. H. V. T., and Conde, C. A. N. 1986 *Nucl. Instrum. Meth. Phys. Res.* A **242**, 327.
[54] Sin Fai Lam, L. T. 1982 *J. Phys.* B **15**, 119.
[55] Schmidt, B. 1991 *J. Phys.* B **24**, 4809.

https://doi.org/10.1017/S0022377805004162 Published online by Cambridge University Press